GeoScienceWorld
Lithosphere
Volume 2023, Article ID 9454084, 12 pages
https://doi.org/10.2113/2023/9454084

Lithosphere

Research Article

Pore Scale Modeling of Capillary Action in Determining Oil–Water Flowing by Water Flooding: A Case Study of Low-Permeability Sandstone in the Ordos Basin, Northern China

Wei Xu,[1] **Tianjiang Wu**,[2] **Chen Cheng**,[2] **Jibo He**,[3] **and Junwei Su**[1]

[1]*Institute of Global Environmental Change, Xi'an Jiaotong University, Xi'an 710049, China*
[2]*Oil & Gas Technology Research Institute, Changqing Oilfield Branch Company, PetroChina, Xi'an 710018, China*
[3]*No.10 Oil Production Plant of Changqing Oilfield Branch of PetroChina, Qingcheng, Gansu 745100, China*

Correspondence should be addressed to Junwei Su; sujunwei@xjtu.edu.cn

Received 23 August 2022; Revised 28 December 2022; Accepted 5 January 2023; Published 17 January 2023

Academic Editor: Qinghai Xu

Copyright © 2023 Wei Xu et al. Exclusive Licensee GeoScienceWorld. Distributed under a Creative Commons Attribution License (CC BY 4.0).

Capillary action plays an important role in oil recovery by water flooding. As the pore channel radius decreases, the capillary action increases, which seriously affects reservoir development, especially in a low-permeability sandstone reservoir. The Ordos Basin is a typical low-permeability sandstone reservoir in China. Studying how variations in the capillary force affect the remaining oil production on the pore scale helps in understanding how the capillary action improves the development of unconventional reservoirs. In this study, the core of the Chang 6 Formation in the Ansai Oilfield, Ordos Basin was scanned by computed tomography. Then, the digital core model was established. The oil–water two-phase flow in pores was described using the method based on the Navier–Stokes equation coupled with the method of the volume of fluid simulation. The water flooding process was simulated on the pore scale. The results show that in the process of pore scale water flooding, the oil–water interface stays at the position between the throat channel and the pore area, where the oil–water interface reverses and the capillary force presents resistance, forming the capillary barrier or capillary valve. Affected by the capillary barrier, the oil–water two-phase flow in the process of water flooding is described by a "step-by-step" model. The pore structure characteristics at the junction of the pore area and the throat channel control the movement of the oil–water interface and affect the water flooding production and the ultimate recovery factor. As the liquid injection rate increases, the oil on both sides of the main channel is produced. While the oil recovery rate reaches 66%, the remaining oil on the edges becomes increasingly difficult to be produced. This difficulty is closely related to the viscosity of the injection fluid, interfacial tension, injection rate, pore radius, and pore wall wettability.

1. Introduction

Waterflood development is the most widely used secondary oil recovery method worldwide, which can keep the reservoir pressure stable and improve oil displacement efficiency. However, the water cut increases continuously with waterflood development and the efficient development of the remaining oil in the stratum becomes a key scientific issue [1]. Although measures such as profile modification, water plugging, and well pattern adjustment can be taken to slow down the rise of water cut [2–4], the water cut still increases. Additionally, most reservoirs in China are continental clastic deposits, accounting for about 92%. They are highly heterogeneous and demonstrate high crude oil viscosity in the longitudinal and horizontal directions, resulting in low oil recovery by water flooding [1]. Currently, most reservoirs in China have entered the mature development stage, with water cuts higher than 80% and recovery rates lower than 30% [5, 6]. Therefore, using existing scientific and technological methods, the industry has focused on how to maximize the efficiency of oil displacement in a high water cut period. The occurrence state and distribution characteristics of the remaining oil in the high water cut stage are closely related to the pore properties of the reservoir. The influence

Downloaded from http://pubs.geoscienceworld.org/gsa/lithosphere/article-pdf/doi/10.2113/2023/9454084/5769152/9454084.pdf
by guest

of microscopic forces such as surface tension and capillary force on the remaining oil production becomes particularly important [7–10]. Particularly in unconventional reservoirs represented by low-permeability reservoirs, coalbed methane reservoirs, and shale reservoirs, the scale of pore and throat channel is small, and the capillary force has a significant impact on the occurrence and production of reservoir fluids [11, 12]. A deep understanding of the capillary action could greatly help improve the development effect of unconventional reservoirs [13, 14].

Currently, the microflow process of water flooding is described by physical and numerical simulations [15–18]. The physical simulations can only derive the distribution law of oil and water in pore space and the characteristics of macroscopic flow and pressure. Owing to measurement limitations, physical simulations are limited in the ability to study the mechanism behind the macrocharacteristics of water flooding. Numerical simulations can quantitatively describe the multiphase flow process in pores and reproduce the movement disciplinarian of oil and water at the pore scale. Over the past few years, numerical simulations have gradually become the new method for studying multiphase flows at the pore scale. To further investigate how the oil–water interface affects the oil–water two-phase flow on the pore scale, it is crucial to accurately determine the position and tension of the oil–water interface. The research methods for interface position tracking include the front tracking method, level set method, and volume of the fluid method [19–21]. The volume of fluid method can be extended from the two to the three dimensions, the volume is conserved in the calculation process, and the interface movement can be accurately tracked by a high-precision solution algorithm or accurate interface reconstruction technology. Open-source Field Operation and Manipulation (OpenFOAM) is a C++ code package that is open source, readable, and expansible [22]. There are many two-phase solvers in OpenFOAM. interFoam is used to solve the insoluble two-phase movement process with a free surface. The Navier–Stokes equation is used to describe the fluid movement, the volume of fluid method is used to solve the position of the two-phase free surface, and the finite volume method is the most perfect and basic two-phase solver in OpenFOAM.

The Ordos Basin, an important oil-bearing basin in the west of the North China Craton, is a typical representative of continental low-permeability reservoirs in China [23–26]. Low porosity and low permeability are the significant characteristics of sandstone reservoirs in the Yanchang Formation. The porosity ranges mainly between 6% and 16%, while the permeability ranges mainly between 0.1 and 3.0 mD [27, 28]. Understanding the intrinsic relationship between capillary action and the characteristics of water flooding for low-permeability reservoirs and providing a theoretical basis for analyzing the formation mechanism and distribution law of the remaining oil is very important.

In this study, the images of the core of the T_3Ch_6 Formation in the Ansai Oilfield, Ordos Basin from computed tomography (CT) scans were used to construct the digital core model to simulate the core structure. Based on the interFoam solver in OpenFOAM, the calculation process uses the Navier–Stokes equation to describe the two-phase medium movement and the volume of fluid method to track the position of the two-phase interface. The pressure implicit with splitting of operators (PISO) algorithm [29] was used to decouple the pressure and velocity equations and simulate the two-phase medium movement. The dynamic positions of oil and water during water flooding with pore size are simulated, and the changes in the capillary force and the influence of the capillary barrier on oil–water movement are analyzed. The analysis of the remaining oil production by increasing the liquid injection rate is also discussed.

2. Geological Setting

The Ordos Basin is the second largest sedimentary basin in China, which is located in the Yinshan Mountain in the north, the Qinling Orogenic Belt in the south, the Lvliangshan Orogenic Belt in the east, and the Liupanshan Thrust Belt in the west (Figure 1). It is currently composed of six first-order tectonic units, including the Yimeng Uplift, the Weibei Uplift, the Jinxi Tectonic Belt, the Yishan Slope, the Tianhuan Depression, and the Western Thrust Zone [30]. It is adjacent to the Hetao basin, the Yinchuan Graben, and the Weihe Basin. The development of the Ordos Basin in the Paleo-Mesozoic can be divided into three evolutionary stages: the divergent boundary craton basin from Cambrian to Early Ordovician, the convergent boundary craton basin from Middle Ordovician to Middle Triassic, and the residual craton basin in the plate from Late Triassic to Early Cretaceous [28, 31]. The present basin is a residual basin that has undergone multiple transformation stages. The basin basement is the Precambrian crystalline metamorphic rock. The Upper Proterozoic–Lower Paleozoic marine carbonate deposition, the Upper Paleozoic marine–continental coal-bearing clastic deposition, the Mesozoic continental fluvial–delta–lacustrine facies deposition, the Cenozoic aeolian loess, and the fluvial facies deposition are deposited on the basement [32]. The total thickness is about 5000–6000 m. The oil-bearing strata in the Ordos Basin are the Yanchang Formation of the Middle–Upper Triassic and the Middle Jurassic Formation, and the gas-producing strata are the Carboniferous–Permian and Ordovician Formations [31]. The Triassic Yanchang Formation is rich in low-permeability reservoirs, and the proven tight oil reserves are about 2.0 billion tons [28]. It mainly occurs in tight sandstone reservoirs of the $T_3Ch_{6\text{-}8}$ oil-bearing intervals nearby or is interbedded with oil shale layers, without migrating to large distances.

The Ansai Oilfield is located in the middle east of the Yishan Slope in the Ordos Basin, and its tectonic setting is a gentle west-dipping monocline [33]. The Ansai Oilfield is a typical low-permeability and low-yield oilfield. Its reservoir is the Yanchang Formation of the Triassic, buried at a depth of 1000–1300 m, and it is a sedimentary system dominated by the delta of an inland freshwater lake [34]. The T_3Ch_6 oil-bearing formation is an important oil-bearing formation in the Wangyao area, which can be divided into $T_3Ch_6^1$, $T_3Ch_6^2$, and $T_3Ch_6^3$ layers. $T_3Ch_6^1$ is the main production

Downloaded from http://pubs.geoscienceworld.org/gsa/lithosphere/article-pdf/doi/10.2113/2023/9454084/5769152/9454084.pdf
by guest

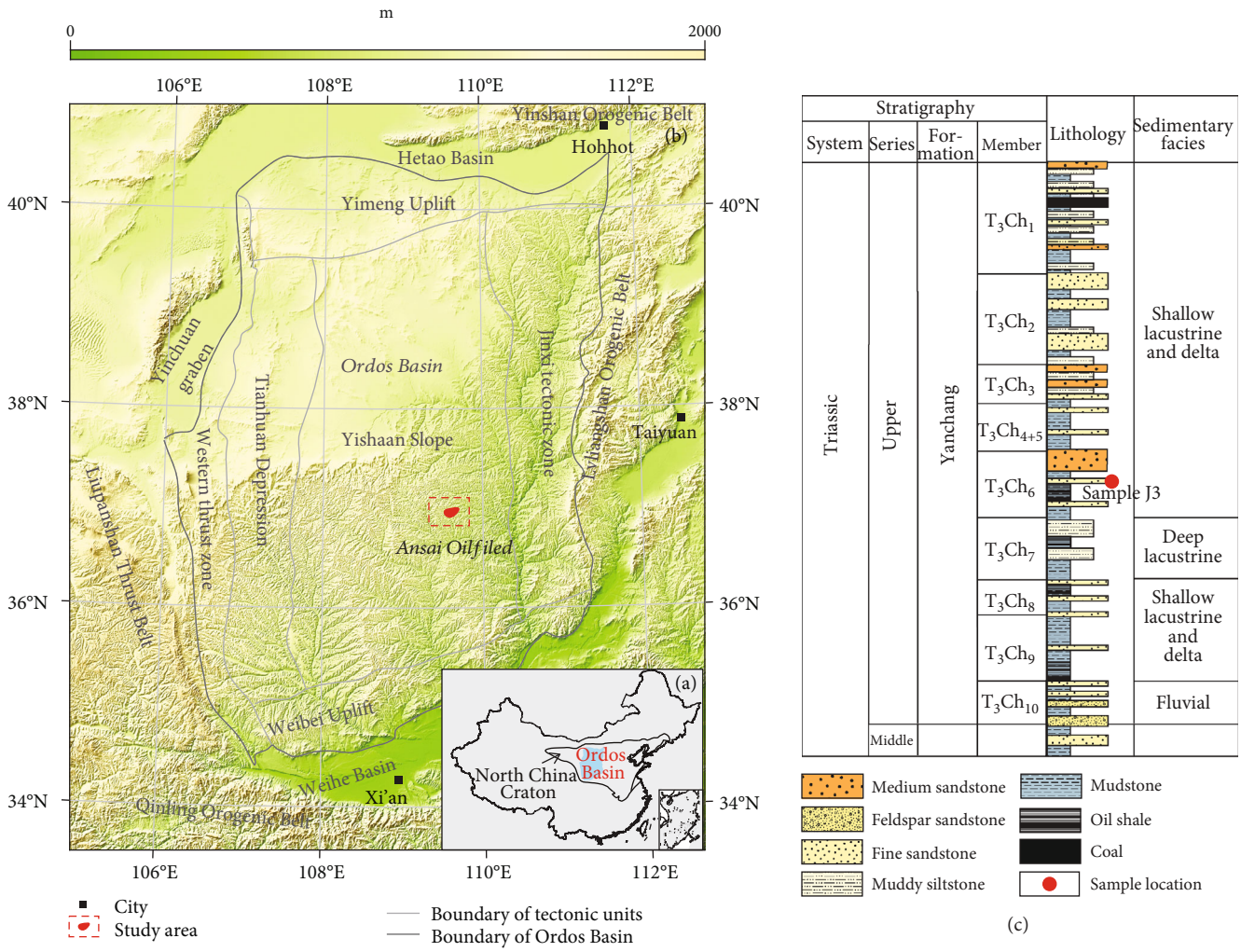

Figure 1: (a) The location map of the Ordos Basin. (b) The tectonic map of the Ordos Basin, data of tectonic unit reference from Yang et al. [30]. (c) Stratigraphic columns of the Yanchang Formation in the Ordos Basin [26].

layer. The average porosity of the T_3Ch_6 reservoir is 13.30%, the average permeability is 2.3 mD, and the average thickness of the oil layer is about 12 m. These data suggest that the reservoir demonstrates low porosity, low permeability, and low production [33].

3. Methods and Parameters

3.1. Pore Scale Numerical Model. In this study, the volume of fluid method is used to track the position of the oil–water interface. The principle is to define a volume fraction α. When α is equal to 0 or 1, it means that the grid cell is occupied by the specified phase fluid or no specified fluid. When α ranges between 0 and 1, the grid cell has a free interface, which is called the interface element. The free surface was determined by tracking the interface position and direction with the volume fraction. In this study, the grid cell is filled with water when α is equal to 1, and the grid cell is filled with oil when α is equal to 0. The pore scale dynamic model of the oil–water two-phase flow in porous media can be constructed by the following equations:

(1) Continuity equation:

$$\nabla \bullet u = 0, \tag{1}$$

where u is the velocity, m s^{-1}

(2) Volume fraction equation:

$$\frac{\partial \alpha}{\partial t} + \nabla \bullet (\alpha u) = 0, \tag{2}$$

where α is the volume fraction

(3) Momentum equation:

$$\frac{\partial \rho u}{\partial t} + \nabla \bullet (\rho u u) - \nabla \bullet (\mu \tau) = -\nabla p + \rho g, \tag{3}$$

Downloaded from http://pubs.geoscienceworld.org/gsa/lithosphere/article-pdf/doi/10.2113/2023/9454084/5769152/9454084.pdf
by guest

where ρ is the fluid density, kg m^{-3}; μ is the dynamic viscosity coefficient, Pa s; P is the dynamic pressure, Pa; and τ is the rate of the strain tensor, s^{-1}

In Equation (3), ρ is the average density of the two-phase mixed fluid, μ is the average dynamic viscosity coefficient of the two-phase fluid, and their expressions are the following:

$$\rho = \alpha\rho_1 + (1-\alpha)\rho_2, \tag{4}$$

$$\mu = \alpha\mu_1 + (1-\alpha)\mu_2, \tag{5}$$

where ρ_1 is the density of phase 1, kg m^{-3}; ρ_2 is the density of phase 2, kg m^{-3}; μ_1 is the dynamic viscosity coefficient of phase 1, Pa S; μ_2 is the dynamic viscosity coefficient of phase 2, Pa S; α is the volume fraction of phase 1, which is explicitly tracked by Equation (2) in the calculation process.

3.2. Solving Algorithm of the Pore Scale Numerical Model

3.2.1. Finite Volume Discretization Method. The basic idea of computational fluid dynamics is to discretize continuous partial differential equations in grid cells and then solve the simplified algebraic equations to obtain the relevant variables. The commonly used numerical discretization methods include the finite volume method, finite difference method, and finite element method. The finite volume method satisfies the law of conservation of mass, is accurate, and can handle the meshing problem of the complex boundary area. Therefore, using the finite volume discretization method, this study discretized the partial differential equations composed of Equations (1), (2), and (3) and obtained the linear algebraic equations.

In the discretization process of the equation using the finite volume method, for any partial differential equation,

$$\frac{\partial\varphi}{\partial t} + \nabla\cdot(\mathbf{u}\varphi) - \nabla\cdot\left(D_\varphi\nabla\varphi\right) = S_\varphi, \tag{6}$$

where φ is relevant physical quantity; D_φ is the diffusion coefficient; t is the time, s; $\mathbf{u}$ is the velocity, m s^{-1}; and S_φ is a source item.

By integrating Equation (6), we can get

$$\int_V \frac{\partial\varphi}{\partial t}dV + \int_V \nabla\cdot(\mathbf{u}\varphi)dV - \int_V \nabla\cdot\left(D_\varphi\nabla\varphi\right)dV = \int_V S_\varphi dV. \tag{7}$$

According to Gauss's theorem,

$$\frac{\partial\varphi}{\partial t}V + \oint_S u\varphi\cdot dS - \oint_S D_\varphi\nabla\varphi = V\left(S_p\varphi + S_u\right), \tag{8}$$

where V is the volume of the control unit, S_P is the linearization coefficient of the source item S_φ, and S_u is the linearization constant of the source item S_φ.

The finite volume discretization method divides the calculation area into multiple control units containing multiple surfaces. Each surface is composed of a sequence of points. The physical and geometric properties of the surfaces are obtained through a series of point calculations. After discretizing the control units, the following results are obtained:

$$\frac{\varphi_p^{n+1} - \varphi_p^n}{\Delta t}V + \sum_f\left[\mathbf{u}_f\cdot\mathbf{S}_f\right]\varphi_f - \sum_f\left[D_\varphi\left(\nabla\varphi_f\right)\cdot\mathbf{S}_f\right] = V\left(S_p\varphi + S_u\right), \tag{9}$$

where φ_P^{n+1} is the value of a physical quantity at time $n+1$, φ_P^n is the value of a physical quantity at time n, u_f is the speed on the grid cell surface, φ_f is the value of a physical quantity in the element surface, and S_f is the area vector of the element face.

The convection term in Equation (9), namely, the second term on the left, is interpolated:

$$\sum_f\left[\mathbf{u}_f\cdot\mathbf{S}_f\right]\varphi_f = \psi_f\sum_f\left[W_f\varphi_p^{n+1} + \left(1-W_f\right)\varphi_{\text{neighbour},f}^{n+1}\right], \tag{10}$$

$$\psi_f = \mathbf{u}_f\cdot\mathbf{S}_f, \tag{11}$$

$$\varphi_f = W_f\varphi_p^{n+1} + \left(1-W_f\right)\varphi_{\text{neighbour},f}^{n+1}, \tag{12}$$

where ψ_f is the flow rate on the element surface, $W_f$is the weight coefficient of linear interpolation, and $\varphi_{\text{neighbour},f}^{n+1}$ is the value of a physical quantity on the adjacent element at time $n+1$.

The diffusion term in Equation (9), namely, the third term on the left, is interpolated as follows:

$$\begin{aligned}\sum_f\left[D_\varphi\left(\nabla\varphi_f\right)\cdot\mathbf{S}_f\right] &= \sum_f\left[D_\varphi\Delta\varphi^{n+1}\frac{r_{\text{neighbour},f} - r_p}{\left|r_{\text{neighbour},f} - r_p\right|^2}\cdot\mathbf{S}_f\right] \\ &= \sum_f\left[\Delta\varphi^{n+1}\beta_f\right],\end{aligned} \tag{13}$$

$$\Delta\varphi^{n+1} = \varphi_{\text{neighbour},f}^{n+1} - \varphi_p^{n+1}, \tag{14}$$

$$\beta_f = \frac{\left|\mathbf{S}_f\right|D_\varphi}{\left|r_{\text{neighbour},f} - r_p\right|}\Delta\varphi^{n+1}, \tag{15}$$

where $r_{\text{neighbour},f}$ is the position of the face center of the adjacent unit, r_p is the location of the cell center, $\Delta\varphi^{n+1}$ is the difference between a physical quantity on the adjacent element surface and the core of the element body at time $n+1$; and β_f is a physical quantity obtained by linear interpolation, which can be obtained by linear interpolation.

Substituting Equations (10) and (13) into Equation (9), the formula is obtained as follows:

$$\frac{\left(\varphi_p^{n+1} - \varphi_p^n\right)V}{\Delta t} + \psi_f\sum_f\varphi_f - \sum_f\left[\Delta\varphi^{n+1}\beta_f\right] = V\left(S_p\varphi + S_u\right). \tag{16}$$

Downloaded from http://pubs.geoscienceworld.org/gsa/lithosphere/article-pdf/doi/10.2113/2023/9454084/5769152/9454084.pdf
by guest

Further, simplification Equation (16) results in the following:

$$a_p\varphi_p^{n+1} = \sum_f \left[a_{N,f}\varphi_{\text{neighbour},f}^{n+1}\right] + \frac{V}{\Delta t}\varphi_p^n + VS_u, \tag{17}$$

$$a_p = \frac{V}{\Delta t} + \sum_f \psi_f W_f - \sum_f \beta_f - VS_p, \tag{18}$$

$$a_{N,f} = -\psi_f\left(1 - W_f\right) + \beta_f, \tag{19}$$

where α_p is the linearization coefficient and $\alpha_{N,f}$ is the linearization coefficient.

Write the organized equation in the form of a system of linear equations:

$$a_p\varphi_p^{n+1} = \sum_f \left[a_{N,f}\varphi_{\text{neighbour},f}^{n+1}\right] + b, \tag{20}$$

$$b = \frac{V}{\Delta t}\varphi_p^n + VS_u, \tag{21}$$

where b is the linearization constant.

3.2.2. Solver Algorithm and Process. There are currently two types of numerical solutions: coupled and separated. The separated method offers a simple and convenient way to calculate solutions and is widely used. The most widely used method for solving fluid problems is the pressure correction method, which includes SIMPLE, SIMPLEC, PISO, and other algorithms [29, 35]. The PISO algorithm can greatly reduce the number of iterations of the unsteady state problem and further improve calculation efficiency. In this study, the PISO algorithm is used to decouple the rate and pressure.

According to the finite volume discretization process of the polyhedral mesh, the momentum Equation (3) is discretized, and the derived semidiscretization scheme is the following:

$$a_p\mathbf{u} = A_H - \nabla p_d - \nabla p_c, \tag{22}$$

where α_p is the upper diagonal value of the coefficient matrix obtained by discretizing Equation (3), P_d is dynamic pressure, P_c is the pressure gradient owing to surface tension, and A_H is presented as

$$A_H = \sum_N a_N\mathbf{u} + b, \tag{23}$$

where α_N is the implicit contribution coefficient of the node next to the current node in the discretization process of Equation (3) and b represents the explicit discrete contributions other than pressure.

Divide both sides of Equation (23) by a_p and arrange the equation as follows:

$$\mathbf{u} = \frac{A_H}{a_p} - \frac{\nabla p_d}{a_p} - \frac{\nabla p_c}{a_p}. \tag{24}$$

The velocity field obtained from Equation (24) should satisfy the continuity equation. Substitute Equation (24) into the continuity Equation (1) and get

$$\nabla \cdot \left(\frac{1}{a_p}\nabla p_d\right) = \nabla \cdot \left(\frac{1}{a_p}A_H\right) - \nabla \cdot \left(\frac{1}{a_p}\nabla p_c\right). \tag{25}$$

The pressure Equation (25) is derived by the PISO algorithm, and the new pressure obtained by solving this equation is substituted into Equation (24) to update the velocity. Additionally, to facilitate the diffusion of convective terms the next time, the flow rate at the interface of the element should be updated at the same time as the velocity at the center of the body. The surface flow rate is updated by the interpolation of Equation (24) on the surface:

$$\varphi_f = \left(\frac{A_H}{a_p}\right)_f \cdot S_f - \nabla \cdot \left(\frac{\nabla p_d}{a_p}\right)_f \cdot S_f - \left(\frac{\nabla p_c}{a_p}\right)_f \cdot S_f, \tag{26}$$

where φ_f is surface flow rate.

In the numerical simulation process of this study, the flow of calculating the solutions of equations is as follows: First, the finite volume method is used for the discrete solution of the momentum Equation (3), and the velocity u is derived. Then, the PISO algorithm is used to derive the pressure Poisson Equation (25), and the volume fraction Equation (2) is solved to obtain the volume fraction at the next moment. Finally, Equations (4) and (5) are used to track the fluid properties. Then, repeat the first step until the end of the cycle is reached or convergence accuracy is achieved.

3.3. Digital Core Model and Parameters. The core sample was drilled in the Ansai Oilfield of the Ordos Basin, whose lithology is sandstone. A cylinder with a diameter of 2.00 mm is cut in the selected area on the core column, and the sample is scanned in a micron CT scanner with a scanning resolution of 0.70 μm.

The micron CT used in this study is the Zeiss Xradia 510 Versa micron CT scanner produced by the Zeiss company. The 3D spatial resolution is less than 0.70 μm, the pixel size of the 40x detector (objective lens) at the maximum magnification is 0.34 μm, and the pixel size of the 20x detector (objective lens) ranges from 0.65 to 0.68 μm. The moving range of the X-ray source is 215.00 mm, and the moving range of the detector is 290.00 mm. Simultaneously, built-in in situ tensile or compression test bench, equipment model DEBEN-CT5000-RT-SS, maximum support 5 kN loading force, and loading speed from 0.03 to 0.30 mm/min. The sample was scanned by a micron CT scanner. The scan results are shown in Figure 2(a). The cross-

Downloaded from http://pubs.geoscienceworld.org/gsa/lithosphere/article-pdf/doi/10.2113/2023/9454084/5769152/9454084.pdf
by guest

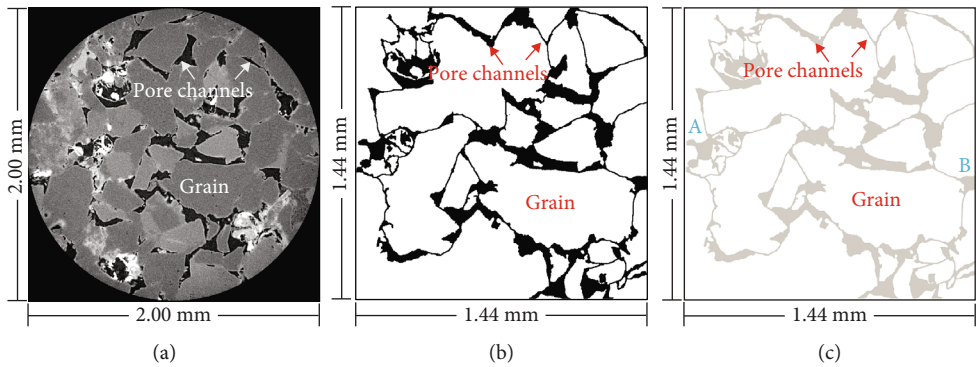

Figure 2: (a) Micron CT scan results of J3 sample (core diameter 2.00 mm, gray area are grains, dark area are pore channels). (b) Binary map from CT image of J3 sample (size: 1.44 mm × 1.44 mm). (c) Digital core model (A is the inlet of water injection, B is water outlet).

Table 1: Numerical boundary conditions.

Boundary	Filed	Type of boundary conditions	Remark
Inlet (A)	Velocity (U)	Fixed value	
	Pressure (p)	Zero gradient	
	Water saturations (alpha)	Fixed value	Value = 1 indicates water injection
Outlet (B)	Velocity (U)	Zero gradient	
	Pressure (p)	Fixed value	
	Water saturations (alpha)	Zero gradient	
Wall	Velocity (U)	Fixed value	Velocity is (0, 0, 0)
	Pressure (p)	Fixed flux pressure	
	Water saturations (alpha)	Alpha constant angle	

section obtained by scanning indicates that the clastic particles have medium-poor sorting, poor roundness, and general pore connectivity, belong to a grain-support structure. The local quartz particles are sutured contacts. According to the scanned data, image segmentation is performed to obtain the image binary map (Figure 2(b)). Based on this, the pore network model can be established to calculate pore throat parameters and perform seepage flow simulations.

In this study, the digital core model used in the test was selected based on the CT scan data (Figure 2(c)). The physical size of the digital core is 1.44 mm × 1.44 mm, with particles in the white area and pore channels in the gray area. Initially, the core is filled with oil. During the simulation, water is injected into the pore from A on the left, displacing oil in the core, and liquid is drained from B. All other positions are closed. The boundary conditions used in the calculation are shown in Table 1, and the physical conditions of the fluid are shown in Table 2.

4. Results

Water was injected into the core from inlet A at a constant injection rate, and the distribution characteristics of oil and water during water flooding at this injection rate were obtained (Figure 3). The injection rate used in this core model is 0.005 m/s, the capillary number is 7.15×10^{-5}, the oil–water viscosity ratio is 5 : 1, and the wetting angle is 45°.

Table 2: Physical conditions of the fluid.

Media	Physical property	Value
Oil	Kinematic viscosity υ (m^2/s)	6.25×10^{-6}
	Density ρ (kg/m^3)	800
Water	Kinematic viscosity υ (m^2/s)	10^{-6}
	Density ρ (kg/m^3)	1000
Oil–water interface	Interfacial tension σ (kg/s^2)	0.07

Figure 3 shows the oil–water distribution and the positions of the oil–water interface at (a) 0.180 s, (b) 0.230 s, (c) 0.325 s, (d) 0.400 s, (e) 0.465 s, (f) 0.585 s, (g) 0.775 s, (h) 0.820 s, and (i) final. The oil–water interface stays between the throat channel and the pore area, where the throat channel or pore radius changes abruptly. For example, at 0.180 s, the oil–water interface stays at the positions of *a1*, *b1*, and *c1* (Figure 3(a)); at 0.230 s, it stays at position *b2* (Figure 3(b)); at 0.325 s, it stays at positions *b3* and *e1* (Figure 3(c)); at 0.4 s, it stays at positions *e2* and *e3* (Figure 3(d)); at 0.465 s, it stays at positions *b4* and *b5* (Figure 3(e)); at 0.585 s, it stays at position *b6* (Figure 3(f)); at 0.775 s, it stays at positions *e5* and *b7* (Figure 3(g)); at 0.820 s, it stays at positions *b8* and *b9* (Figure 3(h)). In this case, the capillary tension may appear as resistance even under wet conditions.

Downloaded from http://pubs.geoscienceworld.org/gsa/lithosphere/article-pdf/doi/10.2113/2023/9454084/5769152/9454084.pdf
by guest

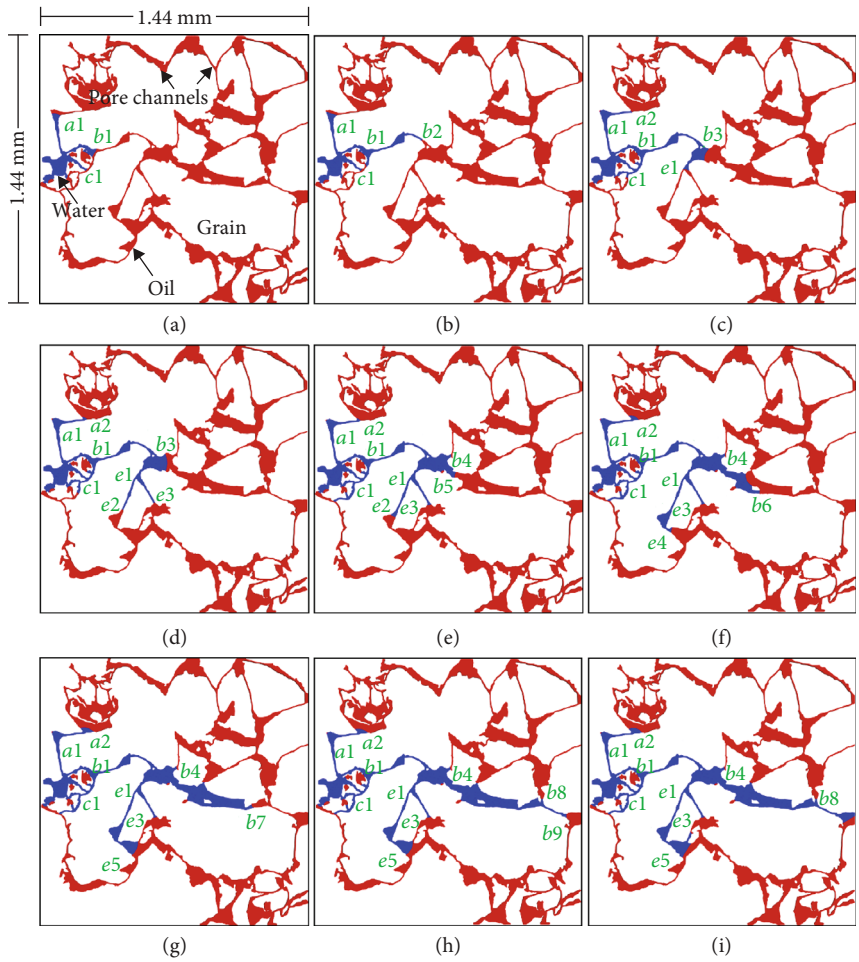

Figure 3: The oil–water distribution and the position of the oil–water interface at different times (injection rate: 0.005 m/s): (a) 0.180 s, (b) 0.230 s, (c) 0.325 s, (d) 0.400 s, (e) 0.465 s, (f) 0.585 s, (g) 0.775 s, (h) 0.820 s, and (i) final. The blue is water, and the red is oil; *a1* and *a2*, *b1*–*b9*, *c1*, and *e1*–*e5* are the positions of the capillary barrier.

5. Discussion

5.1. Variation of Capillary Force in Pore Scale during Water Flooding. During water flooding, the capillary force greatly affects oil and water distribution [15, 18, 36, 37]. The oil–water interface is easy to stop in the area where the radius of the throat channel and pore area changes abruptly (Figure 3).

To explain this phenomenon, we present the morphology of the oil–water interface at different positions and the variation in the capillary force at the corresponding positions (Figure 4). When the oil–water interface is in the throat channel, the direction of the capillary force (pointing to the side of the concave liquid surface) under water-wet conditions is consistent with the direction of the oil–water movement and the capillary force is the power (A $\longrightarrow$ B). When water flows out of the throat channel and $\theta + \beta < \pi/2$ (θ is the three-phase contact antenna of the oil–water–pore, β is the opening angle of the pore), the direction of the oil–water movement remains the same (B $\longrightarrow$ D), but the capillary force gradually decreases from P_c max (Figures 4(a) and 4(b)). When $\theta + \beta > \pi/2$, the oil–water two-phase interface reverses, and the capillary force points to the waterside, preventing oil and water movement (B $\longleftarrow$ D) (Figures 4(c) and 4(d)). After the oil–water interface moves to position B, the oil–water interface only deforms but does not move forward (the three-phase contact line stays at position B) until the angle between the deformed interface and the waterside angle of pore wall equals the equilibrium wetting angle θ (the oil–water morphology *b* is shown in Figure 4(c)). During this process, the capillary force formed on the pore wall of oil–water changes from P_c max to 0 (the oil–water morphology *d* is shown in Figure 4(c)); thereafter, the oil–water interface reverses and the capillary force becomes negative until the negative maximum $P_c$min. When the fluid power is insufficient to overcome this maximum resistance, the oil–water interface stops moving. Therefore, the driving pressure must be higher than the negative maximum $P_c$min to promote the fluid flow. This threshold is called the capillary valve.

Figure 3 shows that water flows into the pore from the left inlet. At 0.180 s, the oil–water interface encounters the capillary barrier at position *b* and stops moving (Figure 3(a)). The effect of the capillary valve is formed here, which causes the lateral spread of oil and water. At 0.230 s, the effect of the capillary valve is formed at positions *a* and *c*,

Downloaded from http://pubs.geoscienceworld.org/gsa/lithosphere/article-pdf/doi/10.2113/2023/9454084/5769152/9454084.pdf
by guest

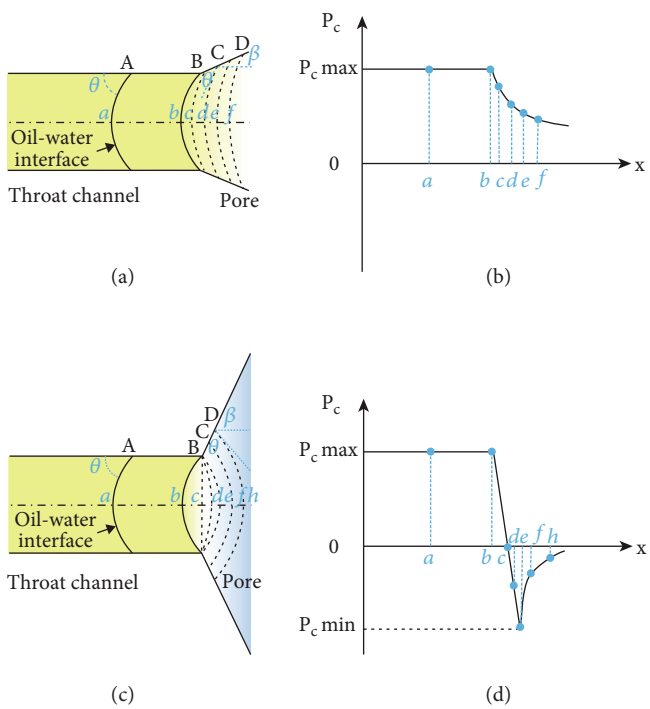

Figure 4: The morphology of the oil–water interface at different positions (a, c) and the capillary force change along the central axis (b, d). When $\theta + \beta < \pi/2$ (a, b), when $\theta + \beta > \pi/2$ (c, d). a–h represent the morphology of the oil–water interface; A–D are the positions of the contact line; θ is the three-phase contact antenna of the oil–water-pore; β is the opening angle of the pore.

preventing further movement of oil and water (Figure 3(b)). After the oil–water interface at positions a and c is blocked, the upstream pressure increases, causing the capillary valve at b to be broken. As a result, the oil–water interface continues to migrate to d and stops at positions f and e at 0.325 s (Figure 3(c)). The blockage at position f causes the oil–water interface to migrate downward and stop at positions g and h at 0.4 s (Figure 3(d)). Simultaneously, water moves further along the center channel and blocks at positions i and h at 0.465 s (Figure 3(e)). This blockage will cause the capillary valves at g and j to be broken and the oil in the $f - j$ channel to be displaced (Figure 3(f)). Then, the water spreads forward along the center at position j and blocks at positions k, g, and j (Figure 3(g)). This lateral blockage will cause the capillary valve at position j of the main channel to break and block at positions l and m at 0.820 s (Figure 3(h)). Finally, the oil–water interface moves forward along the channel where m is located and flows out along the outlet.

5.2. Capillary Barrier and the "Step-by-Step" Model of Oil–Water Movement. During water flooding, the oil–water movement is not stable and continuous, but a "step-by-step" movement, which is related to the capillary barrier (Figures 3, 5 and 6). If a capillary barrier is formed in the flow direction and prevents further movement of the oil–water interface, the oil and water will move laterally. If a capillary barrier forms laterally and prevents further sweep, the water drive front will advance along the main flow direction. Then, the process is repeated, that is, the "step-by-step" oil and water movement. Therefore, the capillary barrier controls the movement model of oil and water and then affects their spatial sweep range.

Figure 5 shows the oil and water "step-by-step" movement and the pressure change after the capillary barrier is formed at positions a, b, and c. After water injection, capillary barriers are formed at points a, b, and c, and the pressure of the oil phase is greater than that of the water phase at the corresponding points (Figures 5(a), 5(d) and 6). If water injection is continuous, the capillary pressure breaks at point c and forms a capillary barrier at point d (Figure 5(b)). With the break of c, the pressure state changes, and the downstream pressure of point a decreases, while the downstream pressures of points b and d increase (Figures 5(e) and 6). The downstream pressure rise will impede fluid movement in the parallel channel. After the pressure barrier forms at point d, the oil–water interface breaks again from point a and forms a capillary barrier at point e (Figure 5(c)). The downstream pressure of the corresponding point a increases again, while the downstream pressures of b and d decrease (Figures 5(f) and 6).

5.3. Analysis of Remaining Oil Production after Increasing Liquid Injection Rate. To investigate how different injection rates affect the degree of the remaining oil production, we simulated the distribution of the remaining oil under five injection rates. First, the core was filled with oil, and then, water was injected into the core from inlet A at rate of 0.005 m/s, with B as the extraction outlet. The oil–water viscosity ratio was set to 5 : 1, while the wetting angle was set to 45°. Other flow parameters are listed in Tables 1 and 2. The water flooding process continues until no oil is produced at outlet B. At this time, the oil and water distribution is shown in Figure 7(a), and the process is shown in Figure 3. Then, water was injected from inlet A at a rate of 0.010 m/s, 0.050 m/s, 0.100 m/s, and 0.500 m/s, respectively. The inlet and outlet positions and the fluid properties remain unchanged when the injection rate increases.

Figure 7 shows the final oil–water distribution driven by water at different injection rates. Figure 7(a) shows the initial state of oil and water distribution with an injection rate (0.005 m/s). Oil and water migrate along Channel 1, and the remaining oil is distributed on both sides of the main channel. The oil–water interface at $a - f$ is at the junction of the pore and throat channel, which forms the capillary barrier. The channel pressure is balanced with the capillary resistance at these interfaces so that the oil–water interface at the upper and lower sides of the main channel is stalled. When water flooding was carried out at a low injection rate (0.010 m/s), the remaining oil was spatially distributed in the lower area of the main channel (Channel 1), and point e was broke, causing a part of the remaining oil to move down along Channel 2, while the upper area did not change (Figure 7(b)). When the injection rate is 0.050 m/s, the pressure increases, exceeding the capillary force at interfaces a and g, so that the capillary barrier at interfaces a and g breaks, and the remaining oil moves to both sides of the main channel along the Channel 3 and Channel 4 (Figure 7(c)).

Downloaded from http://pubs.geoscienceworld.org/gsa/lithosphere/article-pdf/doi/10.2113/2023/9454084/5769152/9454084.pdf
by guest

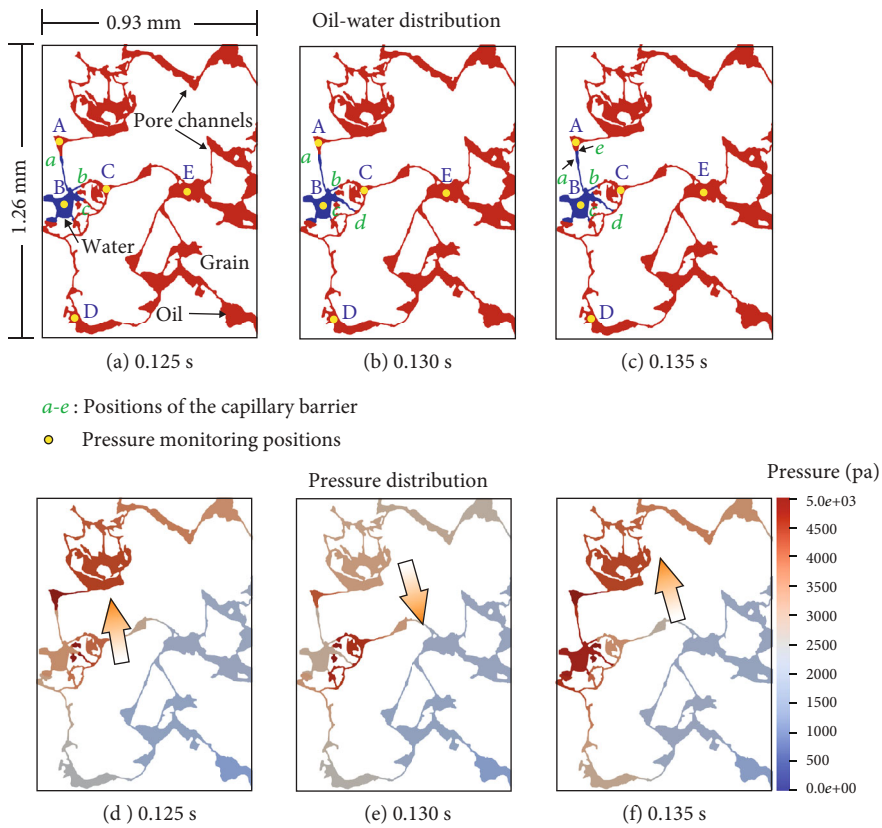

Figure 5: Oil–water distribution induced by capillary barrier ((a) 0.125 s, (b) 0.130 s, and (c) 0.135 s) and pressure distribution induced by capillary barrier ((d) 0.125 s, (e) 0.130 s, and (f) 0.135 s). Arrows represent the direction of pressure increase, a – e are the capillary valve positions; A–E are the pressure monitoring points; the injection rate is 0.005 m/s.

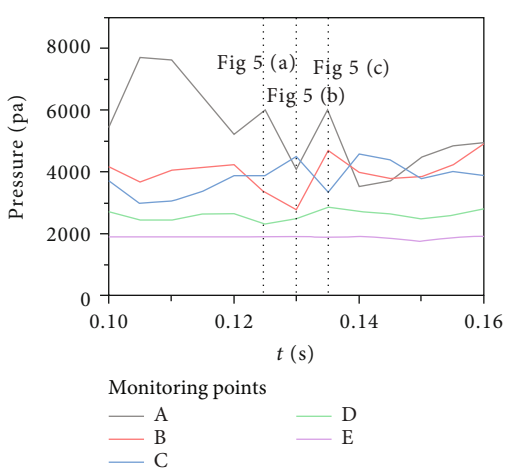

Figure 6: The pressure changes with time for monitoring points (A–E) in Figure 5.

This allows the remaining oil to be produced. Additionally, the existence of an oil block at c blocks the main Channel 1. The pressure on the main channel is balanced with the capillary force at the interface on both sides of the oil block, which is in a stagnant state and drives out the remaining oil at the lower side from the right outlet along Channel 4. When the injection rate increases to 0.100 m/s, the barrier at b is breached, and the remaining oil is produced and moves along Channel 5 (Figure 7(d)). When the injection rate increases to 0.500 m/s, the capillary pressures at c and d on the upper side break, and the capillary valve is formed again at b. The remaining oil on the upper side is produced and moves along Channel 7 and Channel 8, and the barrier at f on the lower side is broken and Channel 6 is formed (Figure 7(e)).

Overall, as the injection rate gradually increases, the oil on both sides of the main channel will be produced successively, and the remaining oil on the edge is becoming increasingly difficult to be produced. The final recovery rate shows that an increase in the injection rate from 0.005 m/s to 0.070 m/s causes the rapid production of the remaining oil and increases the recovery rate to 66% with a linear change (Figure 7(f)). Subsequently, the recovery rate slows down and the remaining oil was increasingly difficult to produce. The recovery rate is only 77% when the extraction rate is 0.500 m/s.

5.4. Mechanical Mechanism of Remaining Oil Production. To quantitatively describe the conditions of the remaining oil production, we analyze the distribution characteristics of oil and water under pore conditions. Figure 8 shows the final oil–water distribution characteristics of water flooding when the injection rate is 0.010 m/s. The main water drive channel (Channel 1) is formed between A and B, and part of the

Downloaded from http://pubs.geoscienceworld.org/gsa/lithosphere/article-pdf/doi/10.2113/2023/9454084/5769152/9454084.pdf
by guest

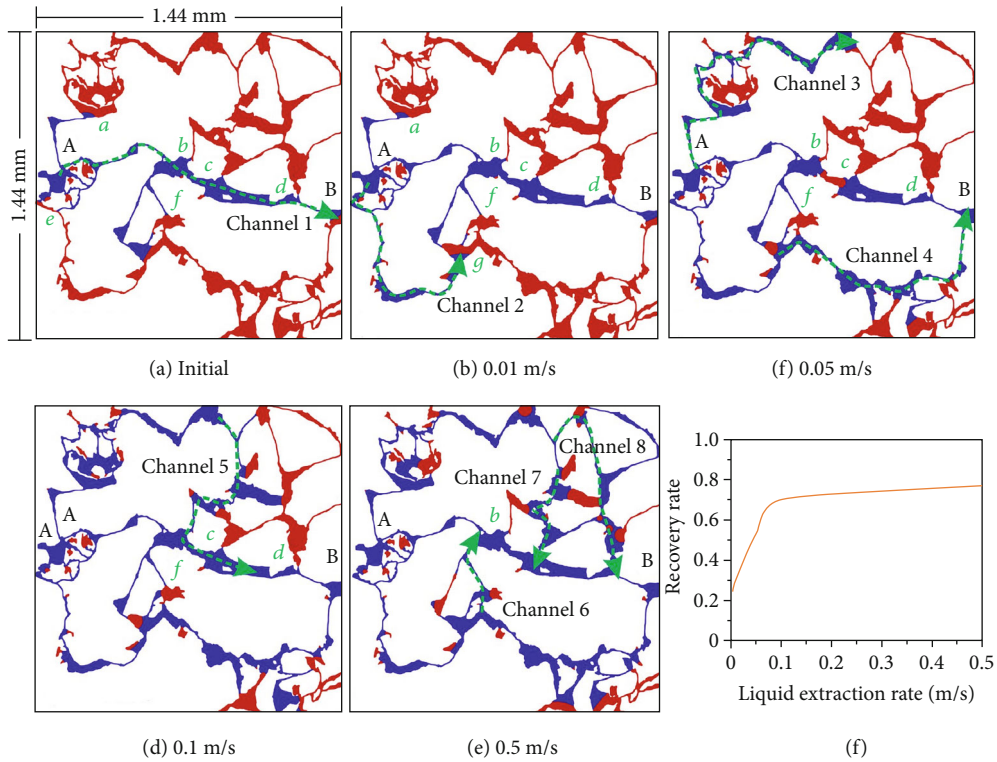

Figure 7: Final oil–water distribution of water flooding with different injection rates ((a) initial, 0.005 m/s; (b) 0.010 m/s; (c) 0.050 m/s; (d) 0.100 m/s; and (e) 0.500 m/s). (f) The recovery curve with increasing liquid injection rate. a – g are the capillary valve positions. Dotted green arrows are the water flooding channels (channels 1–8). A is the inlet of water injection, and B is the water outlet.

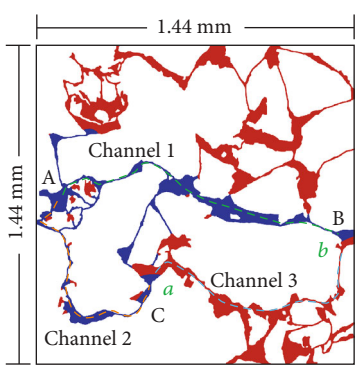

Figure 8: Final oil–water distribution under water flooding conditions with a liquid injection rate of 0.010 m/s. a and b are the positions of the capillary valve. Channels 1–3 are the water flooding channels. A is the inlet of water injection, and B is the water outlet.

remaining oil moves down along Channel 2 (A ⟶ C), while the remaining oil in the upper area is not produced.

The critical condition of the remaining oil production is related to the pressure drop between A and B, and the capillary barrier at a and b. Water in Channel 1 is moving, and there is a pressure drop Δp, which can be expressed by formula (27):

$$\Delta p = \frac{8\mu_w u L}{R_1^2}, \tag{27}$$

where μ_w is water viscosity, u is the injection rate, L is the length of Channel 1, and R_1 is the radius of Channel 1.

A can be connected to B through Channel 2 and Channel 3, but there is no movement of oil and water in these two channels because there are capillary barriers $\Delta p_{a,\text{cap}}$, $\Delta p_{b,\text{cap}}$ at points a and b, respectively, which are expressed by the following formula:

$$\Delta p_{a,\text{cap}} = -\frac{\sigma \cos(\theta + \beta)}{R_2}, \tag{28}$$

$$\Delta p_{b,\text{cap}} = \frac{\sigma \cos(\theta)}{R_3}, \tag{29}$$

where σ is the interfacial tension coefficient, R_2 is the radius of Channel 2, R_3 is the radius of Channel 3, θ is the wetting angle, and β is the opening angle.

If remaining oil from paths A ⟶ C ⟶ B is to be produced, the pressure drop between A and B should be greater than the sum of the capillary barriers at a and b:

$$\Delta p > \Delta p_{a,\text{cap}} + \Delta p_{b,\text{cap}}. \tag{30}$$

By integrating equations (27)–(30), we can obtain

$$u > \frac{\sigma \cos(\theta)}{8R_3\mu_w L} R_1^2 - \frac{\sigma \cos(\theta + \beta)}{8R_2\mu_w L} R_1^2. \tag{31}$$

Downloaded from http://pubs.geoscienceworld.org/gsa/lithosphere/article-pdf/doi/10.2113/2023/9454084/5769152/9454084.pdf
by guest

It can be concluded that if the remaining oil is to be produced, it is necessary to increase the viscosity of water, reduce the interfacial tension, and increase the injection rate. Simultaneously, it is also closely related to the pore radius and the wettability of the pore wall. Changing the wettability may not have an obvious effect on the production of the remaining oil.

6. Conclusions

In this study, a digital core model is established based on CT scan data, and the numerical method used in the simulation process of pore scale water flooding is analyzed. Then, the model of oil–water movement using a constant injection rate is simulated, and the influence of capillary force on oil–water movement during water flooding is discussed.

(1) The oil–water interface stays at the position between the throat channel and the pore area, the oil–water interface reverses, and the capillary force presents resistance, forming the capillary barrier or capillary valve

(2) The oil and water movement during water flooding is not stable and continuous, but a "step-by-step" movement model, which is closely related to the capillary barrier

(3) In the low-permeability sandstone reservoir of the Ansai Oilfield in the Ordos Basin, as the liquid injection rate gradually increases, the oil on both sides of the main channel is successively produced. After the recovery rate reaches 66%, the remaining oil on the edge becomes increasingly difficult to be used

(4) By increasing the viscosity of water, reducing the interfacial tension, and increasing the injection rate to a certain value, the degree of the remaining oil production can be improved. The difficulty of the remaining oil production is closely related to the viscosity of the injection fluid, interfacial tension, influence of injection velocity, pore radius, and wettability of the pore wall

Data Availability

The data that support the findings of this study are available from the corresponding author (Junwei Su) upon reasonable request.

Conflicts of Interest

The authors declare that there is no conflict of interest regarding the publication of this paper.

Acknowledgments

This work is funded by the National Natural Science Foundation of China (No. 12072256) and the Key Research and Development Program of Shaanxi (Program No. 2021GXLH-Z-071).

References

[1] D. Han, "Precisely predicting abundant remaining oil and improving the secondary recovery of mature oilfields," *Acta Petrolei Sinica*, vol. 28, no. 2, p. 73, 2007.

[2] Q. Du, "Variation law and microscopic mechanism of permeability in sandstone reservoir during long-term water flooding development," *Acta Petrolei Sinica*, vol. 37, no. 9, p. 1159, 2016.

[3] Z. Lihong, J. X. Du Qinglong, G. Junhui, W. Liying, J. Yufei, and J. Yinghua, "Characteristics and strategies of three major contradictions for continental facies multi-layered sandstone reservoir at ultra-high water cut stage," *Acta Petrolei Sinica*, vol. 36, no. 2, p. 210, 2015.

[4] Q. Feng, A. Lu, H. Yu, and R. Ma, "A new method for evaluating waterflooding development effectiveness," *Journal-University of Petroleum China Natural Science Edition*, vol. 142, no. 2, pp. 58–60, 2004.

[5] J. Shuhong, C. Tian, C. Shi, Y. Jigen, Z. Zhang, and F. Xiujuan, "New understanding on water-oil displacement efficiency in a high water-cut stage," *Petroleum Exploration and Development*, vol. 39, no. 3, pp. 362–370, 2012.

[6] S. Yuan and Q. Wang, "New progress and prospect of oilfields development technologies in China," *Petroleum Exploration and Development*, vol. 45, no. 4, pp. 698–711, 2018.

[7] J. C. Melrose, "Role of capillary forces in detennining microscopic displacement efficiency for oil recovery by waterflooding," *Journal of Canadian Petroleum Technology*, vol. 13, no. 4, 1974.

[8] Y. Gao, X. Xie, S. Wang, L. Tang, Z. Geng, and J. Li, "Pore-scale experimental investigation of the remaining oil formation in water- wet, mixed-wet and oil-wet sandstone samples," *Journal of Petroleum Science and Engineering*, vol. 216, article 110790, 2022.

[9] J. Li, H. Jiang, C. Wang et al., "Pore-scale investigation of microscopic remaining oil variation characteristics in water-wet sandstone using CT scanning," *Journal of Natural Gas Science and Engineering*, vol. 48, pp. 36–45, 2017.

[10] A. Golparvar, Y. Zhou, K. Wu, J. Ma, and Z. Yu, "A comprehensive review of pore scale modeling methodologies for multiphase flow in porous media," *Advances in Geo-Energy Research*, vol. 2, no. 4, pp. 418–440, 2018.

[11] L. Xiangfang, F. Dong, Z. Tao et al., "The role and its application of capillary force in the development of unconventional oil and gas reservoirs and its application," *Acta Petrolei Sinica*, vol. 41, no. 12, p. 1719, 2020.

[12] S. Wang, F. Javadpour, and Q. Feng, "Confinement correction to mercury intrusion capillary pressure of shale nanopores," *Scientific Reports*, vol. 6, no. 1, 2016.

[13] D. Feng, K. Wu, X. Wang et al., "Effects of temperature and pressure on spontaneous counter-current imbibition in unsaturated porous media," *Energy & Fuels*, vol. 33, no. 9, pp. 8544–8556, 2019.

[14] Z. Sun, X. Li, W. Liu, T. Zhang, M. He, and H. Nasrabadi, "Molecular dynamics of methane flow behavior through realistic organic nanopores under geologic shale condition: pore size and kerogen types," *Chemical Engineering Journal*, vol. 398, article 124341, 2020.

[15] J. Su, G. Chai, L. Wang et al., "Pore-scale direct numerical simulation of particle transport in porous media," *Chemical Engineering Science*, vol. 199, pp. 613–627, 2019.

Downloaded from http://pubs.geoscienceworld.org/gsa/lithosphere/article-pdf/doi/10.2113/2023/9454084/5769152/9454084.pdf
by guest

[16] R. Aziz, V. Joekar-Niasar, and P. Martinez-Ferrer, "Pore-scale insights into transport and mixing in steady-state two-phase flow in porous media," *International Journal of Multiphase Flow*, vol. 109, pp. 51–62, 2018.

[17] A. Zeinijahromi, R. Farajzadeh, J. Hans Bruining, and P. Bedrikovetsky, "Effect of fines migration on oil-water relative permeability during two-phase flow in porous media," *Fuel*, vol. 176, pp. 222–236, 2016.

[18] T. Ning, M. Xi, B. Hu, L. Wang, C. Huang, and J. Su, "Effect of viscosity action and capillarity on pore-scale oil–water flowing behaviors in a low-permeability sandstone waterflood," *Energies*, vol. 14, no. 24, p. 8200, 2021.

[19] S. O. Unverdi and G. Tryggvason, "A front-tracking method for viscous, incompressible, multi-fluid flows," *Journal of Computational Physics*, vol. 100, no. 1, pp. 25–37, 1992.

[20] O. Ubbink, "Numerical prediction of two fluid systems with sharp interfaces, [Ph. D thesis]," Department of Mechanical Engineering Imperial College of Science, Technology & Medicine, 1997.

[21] E. Olsson and G. Kreiss, "A conservative level set method for two phase flow," *Journal of Computational Physics*, vol. 210, no. 1, pp. 225–246, 2005.

[22] H. Jasak, A. Jemcov, and Z. Tukovic, "Openfoam: a c++ library for complex physics simulations," in *International workshop on coupled methods in numerical dynamics*, vol. 1000, pp. 1–20, IUC, Dubrovnik Croatia, 2007.

[23] W. Zhang, H. Yang, J. Li, and J. Ma, "Leading effect of high-class source rock of chang 7 in Ordos basin on enrichment of low permeability oil-gas accumulation-hydrocarbon generation and expulsion mechanism," *Petroleum Exploration and Development*, vol. 33, no. 3, pp. 289–293, 2006.

[24] C. Jia, M. Zheng, and Y. Zhang, "Unconventional hydrocarbon resources in China and the prospect of exploration and development," *Petroleum Exploration and Development*, vol. 39, no. 2, pp. 139–146, 2012.

[25] H. Yang, X. Liu, C. Zhang, T. Y. Han, and X. Hui, "The main controlling factors and distribution of low permeability lithologic reservoirs of Triassic Yanchang formation in Ordos basin," *Lithologic Reservoirs*, vol. 19, no. 3, pp. 1–6, 2007.

[26] Y. Yang, W. Li, and L. Ma, "Tectonic and stratigraphic controls of hydrocarbon systems in the Ordos basin: a multicycle cratonic basin in Central China," *AAPG Bulletin*, vol. 89, no. 2, pp. 255–269, 2005.

[27] S. B. Feng, X. B. Niu, F. Liu et al., "Characteristics of Chang7 tight oil reservoir space in Ordos basin and its significance," *Journal of Central South University (Science and Technology)*, vol. 44, no. 11, pp. 4574–4580, 2013.

[28] J. Yao, X. Deng, Y. Zhao, T. Han, M. Chu, and J. Pang, "Characteristics of tight oil in Triassic Yanchang formation, Ordos basin," *Petroleum Exploration and Development*, vol. 40, no. 2, pp. 161–169, 2013.

[29] P. J. Oliveira and R. I. Issa, "An improved PISO algorithm for the computation of buoyancy-driven flows," *Numerical Heat Transfer, Part B: Fundamentals*, vol. 40, no. 6, pp. 473–493, 2001.

[30] P. Yang, Z. Ren, R. Zhou et al., "Tectonic evolution and controls on natural gas generation and accumulation in the Ordovician system of the Ordos basin, North China," *Energy Reports*, vol. 7, pp. 6887–6898, 2021.

[31] C. Liu, H. Zhao, X. Gui, L. Yue, J. Zhao, and J. Wang, "Space-time coordinate of the evolution and reformation and mineralization response in Ordos basin," *Acta Geologica Sinica*, vol. 80, no. 5, pp. 637–646, 2006.

[32] Z. Zhao, Y. Guo, Y. Wang, and D. Lin, "Study progress in tectonic evolution and paleogeography of Ordos basin," *Tezhong Youqicang-Special Oil & Gas Reservoirs*, vol. 19, no. 5, pp. 15–20, 2012.

[33] H. H. Quan, Y. S. Zhu, H. J. Zhang, L. Li, F. Shao, and Z. Zhang, "Reservoir pore structure and micro-flow characteristics of waterflooding: a case study from Chang-6 reservoir of Wangyao block in Ansai oilfield," *Oil and Gas Geology*, vol. 32, no. 54, pp. 952–956, 2011.

[34] Y. Zhu, Z. Qu, and L. Kong, "Analysis of oil displacement efficiency of chang6 reservoir in Wangyao and Pingqiao areas of Ansai oilfield," *Acta Sedimentologica Sinica*, vol. 18, no. 2, pp. 279–283, 2000.

[35] D. S. Jang, R. Jetli, and S. Acharya, "Comparison of the PISO, simpler, and SIMPLEC algorithms for the treatment of the pressure-velocity coupling in steady flow problems," *Numerical Heat Transfer*, vol. 10, no. 3, pp. 209–228, 1986.

[36] S. Timung, V. Tiwari, A. K. Singh, T. K. Mandal, and D. Bandyopadhyay, "Capillary force mediated flow patterns and non-monotonic pressure drop characteristics of oil-water microflows," *The Canadian Journal of Chemical Engineering*, vol. 93, no. 10, pp. 1736–1743, 2015.

[37] S. Zhang, C. Yu, J. Su, and D. Liu, "Splicing method of micro-nano-scale pore radius distribution in tight sandstone reservoir," *Energies*, vol. 15, no. 5, p. 1642, 2022.

Downloaded from http://pubs.geoscienceworld.org/gsa/lithosphere/article-pdf/doi/10.2113/2023/9454084/5769152/9454084.pdf
by guest